Carbonic Anhydrase IX-Targeted Fluorescence and Nuclear Imaging Agents

Subjects: Radiology, Nuclear Medicine & Medical Imaging

Contributor: Kuo-Ting Chen, Yann Seimbille

Nuclear imaging is a powerful tool for the non-invasive diagnosis of primary and metastatic Carbonic anhydrase IX (CAIX)-positive tumors and for the assessment of responses to antineoplastic treatment. Intraoperative optical fluorescence imaging provides improved visualization for surgeons to increase the discrimination of tumor lesions, allowing for safer surgical treatment. Many CAIX-targeted molecular imaging probes, based on monoclonal antibodies, antibody fragments, peptides, and small molecules, have been reported.

Keywords: carbonic anhydrase IX ; PET ; SPECT ; fluorescence imaging

1. Antibody-Based Imaging Agents

Monoclonal antibodies (mAb) are widely used in the field of imaging because of their excellent target specificity and low uptake in nontarget tissues. The high molecular weight of mAbs allows labeling with dyes and radiometal–chelator complexes without significant loss of their immunoreactivity. However, it may lead to suboptimal penetration into solid tumors. G250 and its chimeric form cG250 (girentuximab) are the most clinically investigated Carbonic anhydrase IX (CAIX) -targeted mAbs. They exhibit high affinity to the extracellular proteoglycan (PG)-like domain of the enzyme, and the PG-like domain only exists in CAIX. They both have high selectivity toward CAIX over other CA isomers [1]. Many radiolabeled girentuximab derivatives have been reported for imaging and treatment of VHL-mutation-induced ccRCC. In 1993, Oosterwijk et al. first reported a phase I with [^{131}I]I-labeled G250 [2]. In the 16 preoperative patients who received 8.4~12.9 mCi of [^{131}I]I-labeled G250 at 5 dose levels, 12 CAIX-positive patients positively responded to the treatment, but one CAIX-negative patient showed a false-positive result. The radiotracer uptake by CAIX-positive tumors was observed in a broad range (0.02 to 0.12% ID/g). In positron emission tomography (PET) imaging, Divgi et al. labeled the chimeric cG250 with the positron-emitter ^{124}I and conducted 2 clinical trials to assess its suitability for ccRCC imaging [3]. The chimeric cG250 showed bioactivity similar to that of G250. In phase I, 26 patients received a single dose of 185 MBq/10 mg of [^{124}I]I-girentuximab 1 week before surgical resection by laparotomy. Patients were followed by PET/CT scanning of the abdomen 3 h prior to the surgery. Their results showed that 15 of 16 ccRCCs were accurately identified by the [^{124}I]I-mAb immuno-PET (sensitivity: 94%), and 9 non-ccRCCs (e.g., papillary RCC, angiomyolipoma and so on) were not detected by the tracer; the negative predictive value (NPV) and positive predictive value (PPV) were 90% and 100%, respectively. Phase III is with 226 preoperative patients, which reported a sensitivity, PPV, and NPV of [^{124}I]I-girentuximab for detecting ccRCC of 86%, 94%, and 70%, respectively. However, the sensitivity was lower for tumor sizes smaller than 2 cm (70.8%) [4]. Parallel to the development of [^{124}I]I-girentuximab, another radiometal-labeled [^{111}In]In-DTPA-cG250 was evaluated in a clinical setting by Muselaers et al. [5]. A total of 29 patients were enrolled in the trial and received 100–200 MBq of [^{111}In]In-DTPA-cG250 4–7 days before single-photon emission computerized tomography (SPECT) scans were performed. The detection rate of the [^{111}In]In-DTPA-cG250 immuno-SPECT was high (PPV = 94%). A total of 15 of 16 cases of ccRCC were successfully identified, and none of the 9 patients with non-ccRCC lesions showed tracer uptake. It is worth noting that, in addition to the detection of primary ccRCC, the [^{111}In]In-DTPA-cG250 was able to detect more metastatic lesions than ^{131}I-cG250 [6]. Very recently, Merkx et al. reported a phase I to evaluate the safety, biodistribution, and dosimetry of [^{89}Zr]Zr-girentuximab [7]. A total of 10 patients with suspected ccRCC received 37 MBq of [^{89}Zr]Zr-girentuximab at mass doses of 5 or 10 mg prior to PET/CT scans at 0.5–168 h post-administration. In most patients, the tumor lesions were visible after 24 h post-administration (PA), and in one case, the tumor could be detected as early as 0.5 h PA. (**Figure 1**). Overall, the [^{89}Zr]Zr-immuno PET was safe and allowed for the successful differentiation between ccRCC and non-ccRCC lesions (6 ccRCC-positive patients; 4 negative scans of non-ccRCC patients). Phase III with [^{89}Zr]Zr-girentuximab is planned to assess the diagnostic accuracy in patients (NCT03849118).

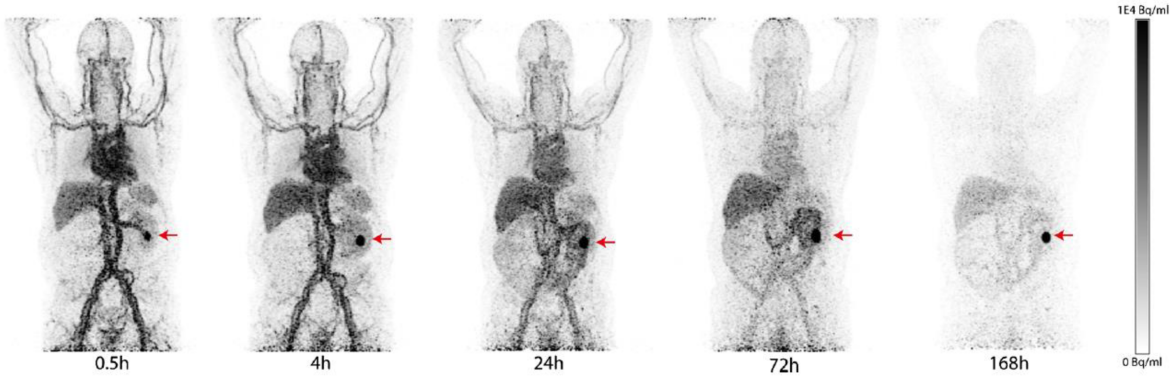

Figure 1. PET/CT imaging of a patient with a ccRCC tumor in the left kidney (red arrow) after injection of [^{89}Zr]Zr-girentuximab. The patient received a mass dose of 10 mg of girentuximab and was imaged at 0.5 to 168 h PA. Tumor-to-background ratio was increased over time.

In addition to the radiolabeled girentuximab, Muselaers et al. developed a dual-modality [^{125}I]I-girentuximab-IRDye800CW and performed preclinical evaluation in mice bearing CAIX-positive SKRC-52 tumors [8]. The mice were imaged at 1 and 3 d post-injection (PI) of [^{125}I]I-girentuximab-IRDye800CW. The results showed an excellent concordance between the micro-SPECT and optical imaging. The tumors were clearly visualized at 24 h PI, and the tumor uptake was 6.9% ID/g at 72 h PI. However, the uptake was lower compared to [^{125}I]I-girentuximab (14.8% ID/g, 72 h PI), which may be due to the faster clearance of the IRDye800CW conjugated antibody. Shortly thereafter, the same group performed dual-modality imaging with [^{111}In]In-DTPA-G250-IRDye800CW in a ccRCC mouse model [9]. The SPECT and fluorescence images showed good concordance and clear delineation of the ccRCC lesions at 48 h PI. The maximum tumor uptake was high, up to 58.5% ID/g at 168 h PI. The promising results of the preclinical evaluation of this dual-modality probe have led to the initiation of a phase I clinical one to assess its feasibility and safety in ccRCC patients. In 2018, a phase I dose-escalation one of [^{111}In]In-DOTA-girentuximab-IRDye800CW in 15 patients with primary renal lesions was performed by Hekman et al. [10] The dual-modality probe (5, 10, 30, or 50 mg) was administered to patients, and SPECT/CT was performed at 4 d PI. The probe showed high sensitivity; all CAIX-expressing tumors were visualized by SPECT/CT, while no uptake was observed in CAIX-negative tumors. Excellent concordance between the SPECT/CT and the near-infrared fluorescence imaging (NIRF) imaging was also observed. During surgery, all ccRCC could be localized by gamma probe measurements with a mean T:N ratio of 2.5 at all protein doses. The optimal T:N ratio (3.3) was found at the 10 mg protein dose, but in general, the protein dose did not significantly affect the T:N ratio (average: 2.5). The phase I was showed that [^{111}In]In-DOTA-girentuximab-IRDye800CW is safe for CAIX-targeted, dual-modality imaging, and it can be used for intraoperative guidance of ccRCC resection.

However, full-size monoclonal antibodies have relatively poor tumor penetration and slow blood clearance, thus requiring a long time to reach the best signal-to-background ratio. In radio imaging, radiation dose accumulation due to the prolonged circulation of the radiotracers in the body could cause a burden for the patients. Antibody fragments with lower molecular weights tend to have rapid localization in tumors. Various types of antibody fragments, such as F(ab')$_2$ (~100 kD), nanobody (~15 kD), and affibody (~7 kD), have been developed to overcome this circumstance. Hoeben et al. reported the use of [^{89}Zr]Zr-DFO-cG250-F(ab')$_2$ as a PET marker of hypoxia in a head and neck xenograft tumor model (SCCNij-3) [11]. The cG250-F(ab')$_2$ was prepared using an enzymatic digestion method. The maximal tumor uptake (3.71% ID/g) of the tracer was found at 4 h PI, but normal tissues (blood, kidney, and liver) also exhibited high uptake of the tracer. The [^{89}Zr]Zr-cG250-F(ab')$_2$ demonstrated specific imaging of CAIX-expressing tumors. Prompted by the results, Huizing et al. performed a preclinical validation of the [^{111}In]In-labeled cG250-F(ab')$_2$ [12]. The specific tracer accumulation (4.1% ID/g) was reached at 24 h PI, and the tumor-to-blood (T/B) and tumor-to-muscle (T/M) ratios of [^{111}In]In-DTPA-cG250-F(ab')$_2$ were 30.8 and 12.1, respectively. However, tracer uptake in the kidneys (65% ID/g) was still high, which may be caused by renal tubular reabsorption. Although high kidney uptake is not a limitation in the case of head and neck tumors, it could interfere with the imaging of tumor masses near the kidney. The probe is therefore not optimal for the detection of CAIX-positive renal cancers. Following the previous research, the protein dose, timing, and image acquisition of [^{111}In]In-DTPA-cG250-F(ab')$_2$ were optimized for a quantitative SPECT imaging analysis of HNSCCs [13]. A protein dose of 10 µg showed the highest tumor uptake of 3.0% ID/g at 24 PI, which is in line with the quantitative microSPECT imaging results (Pearson correlation coefficient (r) = 0.78). In addition, [^{111}In]In-DTPA-cG250-F(ab')$_2$ has been used to monitor the quantitative change in CAIX expression in tumor therapy [14]. Huizing et al. detected a 69% decrease of CAIX levels in a FaDu tumor model after treatment by Atovaquone. However, SPECT imaging with [^{111}In]In-DTPA-cG250-F(ab')$_2$ did not discriminate between the treated and control tumors. According to the authors, the uptake by the treated tumors may also contribute to the Atovaquone-induced enhanced permeability and retention effect (EPR),

which causes it to fail in the application of therapy monitoring. Using smaller biovectors, such as nanobodies or affibodies, may alleviate the EPR effect.

Besides G250 and its fragments, newly developed nanobodies were applied to CAIX-targeted probe preparation. In 2016, van Brussel et al. developed the CAIX-specific nanobody VHH-B9 by phage display selection [15]. VHH-B9 was conjugated with an IRDye800W dye (B9-IR) and evaluated in a xenograft breast cancer mouse model using ductal carcinoma in situ cells (DCIS). Tumor uptake of the fluorescent tracer was 14.0% ID/g, and the T/M and T/B ratios were 70 and 23, respectively. An optical imaging one of BR-I9 showed clear visualization of CAIX-positive DCIS tumors within 2 h after probe administration. Moreover, the rapid pharmacokinetics and probe stability might provide better imaging contrast than conventional CAIX-IHC for pathologic assessment. Very recently, van Lith et al. reported the [^{111}In]In-labeled VHH-B9 in the absence or presence of an albumin-binding domain (ABD) [16]. The ABD on VHH increased the plasma half-life of the VHH, therefore improving the tumor uptake of the tracer. In the comparison one, it reported by van Lith, the uptake of [^{111}In]In-DTPA-VHH-B9 and [^{111}In]In-DTPA-VHH-B9-ABD were 0.51 and 8.7% ID/g, respectively. Not surprisingly, the tumor was only visualized with [^{111}In]In-DTPA-VHH-B9-ABD in SPECT/CT images. However, the uptake of [^{111}In]In-DTPA-VHH-B9-ABD did not decrease after administration of an excess of VHH, which means that the uptake was not CAIX-specific. The authors concluded that the addition of ABD to B9 did not improve SPECT imaging contrast in head and neck cancer.

Affibodies are small proteins based on non-immunoglobulin scaffolds, and they have been used in CAIX imaging [17]. In 2019, Huizing et al. performed an in vivo comparison of the affibody-based [^{111}In]In-DTPA-ZCAIX:2 and two cG250-based radiotracers in a HNSCC xenograft model [18]. Tracer uptake of [^{111}In]In-DTPA-cG250, [^{111}In]In-DTPA-cG250-F(ab')$_2$, and [^{111}In]In-DTPA-ZCAIX:2 in tumors were 30% ID/g at 72 h PI, 3.0% ID/g at 24 h PI, and 0.32% ID/g at 4 h PI, respectively. The tumors were clearly visualized with [^{111}In]In-DTPA-cG250 and [^{111}In]In-DTPA-cG250-F(ab')$_2$ at 24 and 72 h PI, respectively, but not visible with [^{111}In]In-DTPA-ZCAIX:2. Meanwhile, Garousi et al. reported another comparison one between [^{111}In]In-DTPA-cG250-F(ab')$_2$ and [^{111}In]In-DTPA-ZCAIX:2 in the ccRCC model (SKRC-52) [19]. Unlike the abovementioned results, the tumor uptake of the affibody-based probe (15% ID/g) was higher than that of the F(ab')$_2$-based probe (6% ID/g) at 4 h PI, and both radiotracers were capable of visualizing tumors at 4 h PI In a SPECT imaging study, the contrast was higher with [^{111}In]In-DTPA-ZCAIX:2 than it was with the F(ab')$_2$-based probe. However, the high kidney uptake (392% ID/g) hampers the application of this tracer for the imaging of primary ccRCC tumors, but that does not prevent its use in detecting metastases.

2. Peptide-Based Compounds

Peptides are recognized for being highly selective, efficient, and relatively safe vectors. Peptide-based imaging probes typically have a high binding affinity for the target, specific uptake and retention in the target tissue, and rapid clearance from non-target organs. A significant number of peptides, such as cyclic RGD peptides, somatostatin (SST), gastrin-releasing peptide (GRP), glucagon-like peptide-1 (GLP-1), and neuropeptide-Y (NPY), have been labeled with a wide range of imaging moieties for use as in vivo imaging probes. However, research on CAIX-targeted peptides is still limited. In 2010, Askoxylakis et al. identified a dodecapeptide CaIX-P1 (YNTNHVPLSPKY) that targets the extracellular domain of CAIX via a phage display method [20]. The CaIX-P1 contains a *N*-terminal tyrosine residue that was radiolabeled with $^{125/131}$I, and the radiopeptide was evaluated in vitro and in vivo for binding affinity, specificity, and biodistribution. The binding of [^{125}I]I-CaIX-P1 on CAIX-positive SKRC52, HCT116, and HT-29 cells showed a correlation between cell uptake and CAIX expression, but the IC_{50} values, in the micromolar range, were not satisfying. Biodistribution studies of ^{131}I-CaIX-P1 were performed in SKRC-52 and HCT-116 xenografted mice [20][21]. In both experiments, the T/B ratio was found to be lower than 1 at all time points. The highest contrast in SKRC52 and HCT116 were achieved at 1 h and 2 h PI, respectively, and the tumor uptakes of the tracer decreased over time. The low tumor uptakes could be attributed to the low binding of CaIX-P1 to CAIX and the in vivo peptide degradation (half-life of CaIX-P1: 25 min). Besides, no imaging one of the $^{125/131}$I-CaIX-P1 was presented.

To improve the stability and binding properties of the CAIX-targeted peptide, Rana et al. took advantage of the alanine-scanning method to optimize the amino acid sequence of CaIX-P1. It resulted in the new peptide, CaIX-P1-4-10 (NHVPLSPy) [22]. [^{125}I]I-CaIX-P1-4-10 exhibited a 5.8-fold higher binding affinity than [^{125}I]I-CaIX-P1, and it was stable in serum for 90 min. However, tumor uptake of ^{131}I-CaIX-P1-4-10 was not significantly improved (~2.5% ID/g at 1 h PI), and SKRC-52 tumors could not be distinguished from the background. To improve the isoform selectivity, Rena et al. identified a new linear dodecapeptide PGLR-P1 (NMPKDVTTRMSS), which targets the region of the extracellular proteoglycan (PG)-like domain of CAIX with no homology to other Cas [23]. The [^{125}I]I-labeled PGLR-P1 showed a higher selectivity toward CAIX (1.8% applied dose) and the PGLR domain of CAIX (10% applied dose) than CAII and CAXII (both < 0.1% applied dose). However, a rapid peptide degradation was observed with a serum half-life of approximately 20 min.

Although the authors attempted to improve the stability by transforming the l-peptide to its d-enantiomer, a complete loss of binding affinity was noticed with the modified peptides. In addition, the uptake of [^{125}I]I-PGLR-P1 in SKRC-52 tumor (0.48 ± 0.20% ID/g at 1 h PI) was lower than in most normal tissues. Recently, Jia et al. radiolabeled CaIX-P1-4-10 with ^{18}F via a Cu(I)-catalyzed alkyne–azide cycloaddition (CuAAC) [24]. [^{18}F]F-CaIX-P1-4-10 (**1**) was obtained in an overall radiochemical yield of 35–45% from aqueous [^{18}F]fluoride and >99% radiochemical purity in 70–80 min. MicroPET/CT scans of HT-29-bearing mice allowed for the visualization of the tumor at 1 h PI. The tracer accumulated in the tumor with a mean standardized uptake value (SUV_{mean}) of 0.38 ± 0.03, but the uptake in non-target organs remained high (SUV_{means} of liver and kidneys were 14.21 ± 3.68 and 2.08 ± 0.09, respectively). The high background might be due to the rapid degradation of the tracer in serum (48.5% intact after 3 h).

3. Small-Molecule-Based Compounds

The most diverse and largest class of CAIX-targeted imaging probes is small-molecule-based compounds. Small-molecular CA inhibitors exhibit high target affinity and a short blood half-life, making them attractive candidates for use as imaging agents. Several classes of small molecules are known as effective CA inhibitors, such as sulfonamides, coumarins/sulfocoumarins, phenols, and dithiocarbamates [25][26][27][28]. Among them, the aromatic sulfonamides, such as benzenesulfonamide (BSA), acetazolamide (AAZ), and imidazothiadiazole sulfonamide (IS), have particularly gained great interest in the development of imaging agents. The inhibition mechanism of the sulfonamides is by coordination of zinc ions within the active site; however, the similarity of the active sites of all CA isomers hampers the selectivity of the probes. Therefore, the effects of the diverse structures of CA inhibitors on isoform selectivity is emphasized. Herein, it was summarized the current progress of CAIX-targeted molecular imaging probes focused on aromatic sulfonamides. (**Table 1**).

Table 1. Overview of preclinical evaluation of small-molecule-based CAIX-targeted probes.

Agent	Imaging Modality	Fluorophores/Radioisotopes	Binding Affinity	Selectivity CAII/CAIX	Model	Tumor Uptake	Tumor Visualization	Ref.
1	PET	^{18}F	N/A	N/A	HT-29	SUVmean = 0.38 ± 0.03 at 1 h	Y	[24]
2	FL	FITC	K_i = 24 nM	NA	HT-29	N/A	Y	[29]
3	SPECT	^{99m}Tc	K_i = 58 nM	0.86	HT-29	0.2 ± 0.1% ID/g at 0.5 h	Y	[30]
4	SPECT	^{99m}Tc	IC_{50} = 9 nM	N/A	HeLa	N/A	N/A	[31]
5	SPECT	^{99m}Tc	K_i = 0.22 μM [a]	0.3	HT-29	0.07 ± 0.03% ID/g at 1 h	N/A	[32]
6	SPECT	^{99m}Tc	K_i = 0.037 μM [b]	1.2	HT-29	0.14 ± 0.10% ID/g at 1h	Y	[32]
7	PET	^{18}F	K_i = 45 nM	2.1	HT-29	0.83 ± 0.06% ID/g at 1 h	Y	[33]
8	PET	^{18}F	K_i = 6.6 nM	9.0	HT-29	0.64 ± 0.08% ID/g at 1 h	Y	[34]
9	PET	^{18}F	K_i = 0.22 μM	0.3	HT-29	0.41 ± 0.06% ID/g at 1 h	Y	[35]
10	FL	FITC	N/A	N/A	N/A	N/A	N/A	[36]
11	FL	VivoTag-680	K_i = 7.5 nM	33.1	HT-29	10% ID/g at 24 h	Y	[37]
12	FL	S0456	K_d~10 nM.	N/A	HT-29	FL intensity: 2.5 (a.u.) at 4 h	Y	[38]
13	SPECT	^{99m}Tc	N/A	N/A	SKRC-52	22% IA/g at 3 h	Y	[39]

Agent	Imaging Modality	Fluorophores/Radioisotopes	Binding Affinity	Selectivity CAII/CAIX	Model	Tumor Uptake	Tumor Visualization	Ref.
14	PET	^{18}F	N/A	N/A	4T1 HT-29	4T1: 0.2% ID/g at 30 min HT-29: 0.2% ID/g at 15 min	Y	[40]
15	PET	^{68}Ga	N/A	N/A	N/A	N/A	N/A	[41]
16	FL	S0456	N/A	N/A	HT-29	FL intensity: 1.1 (a.u.) at 4 h	Y	[38]
17	PET	^{68}Ga	N/A	N/A	U87MG	1.5% ID/g at 30 min	Y	[42]
18	SPECT	^{111}In	118 ± 21% initial dose/mg protein	N/A	HT-29	8.71 ± 1.41% ID/g at 24 h	Y	[43]
19	SPECT	^{111}In	IC_{50} = 574 nM	N/A	HT-29	12.32% ID/g at 48 h	Y	[44]
20	FL	IRDye750	k_{a2} = 1.36×10^{-6} RU^{-1} s^{-1}	N/A	SKRC-52	5.3 ± 0.6% ID/g at 24 h	Y	[45]
21	FL	S0456	K_d = 45 nM	N/A	HT-29	Epi-fluorescence: 4.3×10^{7} at 4 h	Y	[46]
22	SPECT	^{99m}Tc	K_i = 57 nM	N/A	HT-29	5% ID/g at 4 h	Y	[47]
23	SPECT	^{111}In	125% initial dose/mg	N/A	HT-29	4.57 ± 0.21% ID/g at 1 h	Y	[48]
25	PET	^{68}Ga	60.4 % initial dose/mg	N/A	HT-29	3.81% ID/g at 1 h	Y	[49]
26	PET	^{68}Ga	859 ± 71.7 % initial dose/mg	N/A	HT-29	0.71 ± 0.06% ID/g at 1 h	N	[50]
27	SPECT	^{99m}Tc	IC_{50} = 38.2 nM	N/A	HT-29	3.44 ± 0.50% ID/g at 1 h	N	[51]
28	SPECT	^{99m}Tc	IC_{50} = 211.6 nM	N/A	HT-29	1.82% ID/g at 1 h	N/A	[52]
29	PET	^{18}F	K_i = 8.5 nM	1.0	HT-29	0.33 ± 0.07% ID/g at 1 h	Y	[34]
30	PET	^{68}Ga	K_i = 10.8 nM	12.7	HT-29	0.81 ± 0.15% ID/g at 1 h	Y	[53]
31	PET	^{68}Ga	K_i = 25.4 nM	1.6	HT-29	1.93 ± 0.26% ID/g at 1 h	Y	[53]
32	PET	^{68}Ga	K_i = 7.7 nM	0.93	HT-29	2.30 ± 0.53% ID/g at 1 h	Y	[53]
33	SPECT	^{111}In	IC_{50} = 108.2 nM	N/A	SKRC-52	34.00 ± 15.16% ID/g at 8 h	Y	[54]
34	PET	^{64}Cu	K_d = 4.22 nM	N/A	U87 MG	3.13 ± 0.26% ID/g at 4 h	Y	[55]
35	FMT-CT/MSOT	IRDye 800CW	N/A	N/A	NPC	N/A	Y	[56]

[a] N/A means not available. [b] The K_i was determined using the ^{nat}Re-labeled analog.

References

1. Uemura, H.; Nakagawa, Y.; Yoshida, K.; Saga, S.; Yoshikawa, K.; Hirao, Y.; Oosterwijk, E. MN/CA IX/G250 as a potential target for immunotherapy of renal cell carcinomas. Br. J. Cancer 1999, 81, 741–746.
2. Oosterwijk, E.; Bander, N.H.; Divgi, C.R.; Welt, S.; Wakka, J.C.; Finn, R.D.; Carswell, E.A.; Larson, S.M.; Warnaar, S.O.; Fleuren, G.J.; et al. Antibody localization in human renal cell carcinoma: A phase I study of monoclonal antibody G250. J. Clin. Oncol. 1993, 11, 738–750.
3. Divgi, C.R.; Pandit-Taskar, N.; Jungbluth, A.A.; Reuter, V.E.; Gonen, M.; Ruan, S.; Pierre, C.; Nagel, A.; Pryma, D.A.; Humm, J.; et al. Preoperative characterisation of clear-cell renal carcinoma using iodine-124-labelled antibody chimeric G250 (124I-cG250) and PET in patients with renal masses: A phase I trial. Lancet Oncol. 2007, 8, 304–310.
4. Divgi, C.R.; Uzzo, R.G.; Gatsonis, C.; Bartz, R.; Treutner, S.; Yu, J.Q.; Chen, D.; Carrasquillo, J.A.; Larson, S.; Bevan, P.; et al. Positron emission tomography/computed tomography identification of clear cell renal cell carcinoma: Results from the REDECT trial. J. Clin. Oncol. 2013, 31, 187–194.
5. Muselaers, C.H.; Boerman, O.C.; Oosterwijk, E.; Langenhuijsen, J.F.; Oyen, W.J.; Mulders, P.F. Indium-111-labeled girentuximab immunoSPECT as a diagnostic tool in clear cell renal cell carcinoma. Eur. Urol. 2013, 63, 1101–1106.
6. Brouwers, A.H.; Buijs, W.C.; Oosterwijk, E.; Boerman, O.C.; Mala, C.; De Mulder, P.H.; Corstens, F.H.; Mulders, P.F.; Oyen, W.J. Targeting of metastatic renal cell carcinoma with the chimeric monoclonal antibody G250 labeled with (131)I or (111)In: An intrapatient comparison. Clin. Cancer Res. 2003, 9, 3953S–3960S.
7. Merkx, R.I.J.; Lobeek, D.; Konijnenberg, M.; Jimenez-Franco, L.D.; Kluge, A.; Oosterwijk, E.; Mulders, P.F.A.; Rijpkema, M. Phase I study to assess safety, biodistribution and radiation dosimetry for (89)Zr-girentuximab in patients with renal cell carcinoma. Eur. J. Nucl. Med. Mol. Imaging 2021, 48, 3277–3285.
8. Muselaers, C.H.; Stillebroer, A.B.; Rijpkema, M.; Franssen, G.M.; Oosterwijk, E.; Mulders, P.F.; Oyen, W.J.; Boerman, O.C. Optical Imaging of Renal Cell Carcinoma with Anti-Carbonic Anhydrase IX Monoclonal Antibody Girentuximab. J. Nucl. Med. 2014, 55, 1035–1040.
9. Muselaers, C.H.; Rijpkema, M.; Bos, D.L.; Langenhuijsen, J.F.; Oyen, W.J.; Mulders, P.F.; Oosterwijk, E.; Boerman, O.C. Radionuclide and Fluorescence Imaging of Clear Cell Renal Cell Carcinoma Using Dual Labeled Anti-Carbonic Anhydrase IX Antibody G250. J. Urol. 2015, 194, 532–538.
10. Hekman, M.C.; Rijpkema, M.; Muselaers, C.H.; Oosterwijk, E.; Hulsbergen-Van de Kaa, C.A.; Boerman, O.C.; Oyen, W.J.; Langenhuijsen, J.F.; Mulders, P.F. Tumor-targeted Dual-modality Imaging to Improve Intraoperative Visualization of Clear Cell Renal Cell Carcinoma: A First in Man Study. Theranostics 2018, 8, 2161–2170.
11. Hoeben, B.A.; Kaanders, J.H.; Franssen, G.M.; Troost, E.G.; Rijken, P.F.; Oosterwijk, E.; van Dongen, G.A.; Oyen, W.J.; Boerman, O.C.; Bussink, J. PET of hypoxia with 89Zr-labeled cG250-F(ab')2 in head and neck tumors. J. Nucl. Med. 2010, 51, 1076–1083.
12. Huizing, F.J.; Hoeben, B.A.W.; Franssen, G.; Lok, J.; Heskamp, S.; Oosterwijk, E.; Boerman, O.C.; Bussink, J. Preclinical validation of (111)In-girentuximab-F(ab')2 as a tracer to image hypoxia related marker CAIX expression in head and neck cancer xenografts. Radiother. Oncol. 2017, 124, 521–525.
13. Huizing, F.J.; Hoeben, B.A.W.; Franssen, G.M.; Boerman, O.C.; Heskamp, S.; Bussink, J. Quantitative Imaging of the Hypoxia-Related Marker CAIX in Head and Neck Squamous Cell Carcinoma Xenograft Models. Mol. Pharm. 2019, 16, 701–708.
14. Huizing, F.J.; Hoeben, B.A.W.; Lok, J.; Boerman, O.C.; Heskamp, S.; Bussink, J. Imaging carbonic anhydrase IX as a method for monitoring hypoxia-related radioresistance in preclinical head and neck cancer models. Phys. Imaging Radiat. Oncol. 2021, 19, 145–150.
15. van Brussel, A.S.; Adams, A.; Oliveira, S.; Dorresteijn, B.; El Khattabi, M.; Vermeulen, J.F.; van der Wall, E.; Mali, W.P.; Derksen, P.W.; van Diest, P.J.; et al. Hypoxia-Targeting Fluorescent Nanobodies for Optical Molecular Imaging of Pre-Invasive Breast Cancer. Mol. Imaging Biol. 2016, 18, 535–544.
16. van Lith, S.A.M.; Huizing, F.J.; Franssen, G.M.; Hoeben, B.A.W.; Lok, J.; Doulkeridou, S.; Boerman, O.C.; Gotthardt, M.; van Bergen En Henegouwen, P.M.P.; Bussink, J.; et al. Novel VHH-Based Tracers with Variable Plasma Half-Lives for Imaging of CAIX-Expressing Hypoxic Tumor Cells. Mol. Pharm. 2022.
17. Garousi, J.; Honarvar, H.; Andersson, K.G.; Mitran, B.; Orlova, A.; Buijs, J.; Lofblom, J.; Frejd, F.Y.; Tolmachev, V. Comparative Evaluation of Affibody Molecules for Radionuclide Imaging of in Vivo Expression of Carbonic Anhydrase IX. Mol. Pharm. 2016, 13, 3676–3687.

18. Huizing, F.J.; Garousi, J.; Lok, J.; Franssen, G.; Hoeben, B.A.W.; Frejd, F.Y.; Boerman, O.C.; Bussink, J.; Tolmachev, V.; Heskamp, S. CAIX-targeting radiotracers for hypoxia imaging in head and neck cancer models. Sci. Rep. 2019, 9, 18898.

19. Garousi, J.; Huizing, F.J.; Vorobyeva, A.; Mitran, B.; Andersson, K.G.; Leitao, C.D.; Frejd, F.Y.; Lofblom, J.; Bussink, J.; Orlova, A.; et al. Comparative evaluation of affibody- and antibody fragments-based CAIX imaging probes in mice bearing renal cell carcinoma xenografts. Sci. Rep. 2019, 9, 14907.

20. Askoxylakis, V.; Garcia-Boy, R.; Rana, S.; Kramer, S.; Hebling, U.; Mier, W.; Altmann, A.; Markert, A.; Debus, J.; Haberkorn, U. A new peptide ligand for targeting human carbonic anhydrase IX, identified through the phage display technology. PLoS ONE 2010, 5, e15962.

21. Askoxylakis, V.; Ehemann, V.; Rana, S.; Kramer, S.; Rahbari, N.N.; Debus, J.; Haberkorn, U. Binding of the phage display derived peptide CaIX-P1 on human colorectal carcinoma cells correlates with the expression of carbonic anhydrase IX. Int. J. Mol. Sci. 2012, 13, 13030–13048.

22. Rana, S.; Nissen, F.; Marr, A.; Markert, A.; Altmann, A.; Mier, W.; Debus, J.; Haberkorn, U.; Askoxylakis, V. Optimization of a novel peptide ligand targeting human carbonic anhydrase IX. PLoS ONE 2012, 7, e38279.

23. Rana, S.; Nissen, F.; Lindner, T.; Altmann, A.; Mier, W.; Debus, J.; Haberkorn, U.; Askoxylakis, V. Screening of a novel peptide targeting the proteoglycan-like region of human carbonic anhydrase IX. Mol Imaging 2013, 12, 7290.

24. Jia, L.; Li, X.; Cheng, D.; Zhang, L. Fluorine-18 click radiosynthesis and microPET/CT evaluation of a small peptide—A potential PET probe for carbonic anhydrase IX. Bioorg. Med. Chem. 2019, 27, 785–789.

25. Angapelly, S.; Sri Ramya, P.V.; Angeli, A.; Supuran, C.T.; Arifuddin, M. Sulfocoumarin-, Coumarin-, 4-Sulfamoylphenyl-Bearing Indazole-3-carboxamide Hybrids: Synthesis and Selective Inhibition of Tumor-Associated Carbonic Anhydrase Isozymes IX and XII. ChemMedChem 2017, 12, 1578–1584.

26. Carta, F.; Aggarwal, M.; Maresca, A.; Scozzafava, A.; McKenna, R.; Masini, E.; Supuran, C.T. Dithiocarbamates strongly inhibit carbonic anhydrases and show antiglaucoma action in vivo. J. Med. Chem. 2012, 55, 1721–1730.

27. Maresca, A.; Carta, F.; Vullo, D.; Supuran, C.T. Dithiocarbamates strongly inhibit the beta-class carbonic anhydrases from Mycobacterium tuberculosis. J. Enzyme Inhib. Med. Chem. 2013, 28, 407–411.

28. Innocenti, A.; Vullo, D.; Scozzafava, A.; Supuran, C.T. Carbonic anhydrase inhibitors: Interactions of phenols with the 12 catalytically active mammalian isoforms (CA I-XIV). Bioorg. Med. Chem. Lett. 2008, 18, 1583–1587.

29. Dubois, L.; Lieuwes, N.G.; Maresca, A.; Thiry, A.; Supuran, C.T.; Scozzafava, A.; Wouters, B.G.; Lambin, P. Imaging of CA IX with fluorescent labelled sulfonamides distinguishes hypoxic and (re)-oxygenated cells in a xenograft tumour model. Radiother. Oncol. 2009, 92, 423–428.

30. Akurathi, V.; Dubois, L.; Lieuwes, N.G.; Chitneni, S.K.; Cleynhens, B.J.; Vullo, D.; Supuran, C.T.; Verbruggen, A.M.; Lambin, P.; Bormans, G.M. Synthesis and biological evaluation of a 99mTc-labelled sulfonamide conjugate for in vivo visualization of carbonic anhydrase IX expression in tumor hypoxia. Nucl. Med. Biol. 2010, 37, 557–564.

31. Lu, G.; Hillier, S.M.; Maresca, K.P.; Zimmerman, C.N.; Eckelman, W.C.; Joyal, J.L.; Babich, J.W. Synthesis and SAR of novel Re/99mTc-labeled benzenesulfonamide carbonic anhydrase IX inhibitors for molecular imaging of tumor hypoxia. J. Med. Chem. 2013, 56, 510–520.

32. Nakai, M.; Pan, J.; Lin, K.S.; Thompson, J.R.; Nocentini, A.; Supuran, C.T.; Nakabayashi, Y.; Storr, T. Evaluation of (99m)Tc-sulfonamide and sulfocoumarin derivatives for imaging carbonic anhydrase IX expression. J. Inorg. Biochem. 2018, 185, 63–70.

33. Pan, J.; Lau, J.; Mesak, F.; Hundal, N.; Pourghiasian, M.; Liu, Z.; Benard, F.; Dedhar, S.; Supuran, C.T.; Lin, K.S. Synthesis and evaluation of 18F-labeled carbonic anhydrase IX inhibitors for imaging with positron emission tomography. J. Enzyme Inhib. Med. Chem. 2014, 29, 249–255.

34. Lau, J.; Liu, Z.; Lin, K.S.; Pan, J.; Zhang, Z.; Vullo, D.; Supuran, C.T.; Perrin, D.M.; Benard, F. Trimeric Radiofluorinated Sulfonamide Derivatives to Achieve In Vivo Selectivity for Carbonic Anhydrase IX-Targeted PET Imaging. J. Nucl. Med. 2015, 56, 1434–1440.

35. Zhang, Z.; Lau, J.; Zhang, C.; Colpo, N.; Nocentini, A.; Supuran, C.T.; Benard, F.; Lin, K.S. Design, synthesis and evaluation of (18)F-labeled cationic carbonic anhydrase IX inhibitors for PET imaging. J. Enzyme Inhib. Med. Chem. 2017, 32, 722–730.

36. Ahlskog, J.K.; Dumelin, C.E.; Trussel, S.; Marlind, J.; Neri, D. In vivo targeting of tumor-associated carbonic anhydrases using acetazolamide derivatives. Bioorg. Med. Chem. Lett. 2009, 19, 4851–4856.

37. Groves, K.; Bao, B.; Zhang, J.; Handy, E.; Kennedy, P.; Cuneo, G.; Supuran, C.T.; Yared, W.; Peterson, J.D.; Rajopadhye, M. Synthesis and evaluation of near-infrared fluorescent sulfonamide derivatives for imaging of hypoxia-induced carbonic anhydrase IX expression in tumors. Bioorg. Med. Chem. Lett. 2012, 22, 653–657.

38. Mahalingam, S.M.; Chu, H.; Liu, X.; Leamon, C.P.; Low, P.S. Carbonic Anhydrase IX-Targeted Near-Infrared Dye for Fluorescence Imaging of Hypoxic Tumors. Bioconjug. Chem. 2018, 29, 3320–3331.
39. Krall, N.; Pretto, F.; Mattarella, M.; Muller, C.; Neri, D. A 99mTc-Labeled Ligand of Carbonic Anhydrase IX Selectively Targets Renal Cell Carcinoma In Vivo. J. Nucl. Med. 2016, 57, 943–949.
40. More, K.N.; Lee, J.Y.; Kim, D.Y.; Cho, N.C.; Pyo, A.; Yun, M.; Kim, H.S.; Kim, H.; Ko, K.; Park, J.H.; et al. Acetazolamide-based -PET tracer: In vivo validation of carbonic anhydrase IX as a sole target for imaging of CA-IX expressing hypoxic solid tumors. Bioorg. Med. Chem. Lett. 2018, 28, 915–921.
41. Chen, K.T.; Nguyen, K.; Ieritano, C.; Gao, F.; Seimbille, Y. A Flexible Synthesis of (68)Ga-Labeled Carbonic Anhydrase IX (CAIX)-Targeted Molecules via CBT/1,2-Aminothiol Click Reaction. Molecules 2018, 24, 23.
42. Shin, U.C.; Choi, J.S.; Beak, Y.J.; Lee, M.W.; Kim, H.S.; Choi, D.W.; Kim, D.G.; Kim, S.W. Development of a (68) Ga-labelled PET tracer for carbonic anhydrase IX-overexpressed tumors using the artificial sweetener saccharin. J. Labelled Comp. Radiopharm. 2021, 64, 129–139.
43. Iikuni, S.; Okada, Y.; Shimizu, Y.; Watanabe, H.; Ono, M. Synthesis and evaluation of indium-111-labeled imidazothiadiazole sulfonamide derivative for single photon emission computed tomography imaging targeting carbonic anhydrase-IX. Bioorg. Med. Chem. Lett. 2020, 30, 127255.
44. Iikuni, S.; Okada, Y.; Shimizu, Y.; Watanabe, H.; Ono, M. Modulation of the Pharmacokinetics of a Radioligand Targeting Carbonic Anhydrase-IX with Albumin-Binding Moieties. Mol. Pharm. 2021, 18, 966–975.
45. Krall, N.; Pretto, F.; Neri, D. A bivalent small molecule-drug conjugate directed against carbonic anhydrase IX can elicit complete tumour regression in mice. Chem. Sci. 2014, 5, 3640–3644.
46. Lv, P.C.; Roy, J.; Putt, K.S.; Low, P.S. Evaluation of a Carbonic Anhydrase IX-Targeted Near-Infrared Dye for Fluorescence-Guided Surgery of Hypoxic Tumors. Mol. Pharm. 2016, 13, 1618–1625.
47. Lv, P.C.; Putt, K.S.; Low, P.S. Evaluation of Nonpeptidic Ligand Conjugates for SPECT Imaging of Hypoxic and Carbonic Anhydrase IX-Expressing Cancers. Bioconjug. Chem. 2016, 27, 1762–1769.
48. Iikuni, S.; Ono, M.; Watanabe, H.; Shimizu, Y.; Sano, K.; Saji, H. Cancer radiotheranostics targeting carbonic anhydrase-IX with (111)In- and (90)Y-labeled ureidosulfonamide scaffold for SPECT imaging and radionuclide-based therapy. Theranostics 2018, 8, 2992–3006.
49. Iikuni, S.; Watanabe, H.; Shimizu, Y.; Nakamoto, Y.; Ono, M. PET imaging and pharmacological therapy targeting carbonic anhydrase-IX high-expressing tumors using US2 platform based on bivalent ureidosulfonamide. PLoS ONE 2020, 15, e0243327.
50. Nakashima, K.; Iikuni, S.; Okada, Y.; Watanabe, H.; Shimizu, Y.; Nakamoto, Y.; Ono, M. Synthesis and evaluation of (68)Ga-labeled imidazothiadiazole sulfonamide derivatives for PET imaging of carbonic anhydrase-IX. Nucl. Med. Biol. 2021, 93, 46–53.
51. Iikuni, S.; Tanimura, K.; Watanabe, H.; Shimizu, Y.; Saji, H.; Ono, M. Development of the (99m)Tc-Hydroxamamide Complex as a Probe Targeting Carbonic Anhydrase IX. Mol. Pharm. 2019, 16, 1489–1497.
52. Iikuni, S.; Kitano, A.; Watanabe, H.; Shimizu, Y.; Ono, M. Synthesis and evaluation of novel technetium-99m-hydroxamamide complex based on imidazothiadiazole sulfonamide targeting carbonic anhydrase-IX for tumor imaging. Bioorg. Med. Chem. Lett. 2020, 30, 127596.
53. Lau, J.; Zhang, Z.; Jenni, S.; Kuo, H.T.; Liu, Z.; Vullo, D.; Supuran, C.T.; Lin, K.S.; Benard, F. PET Imaging of Carbonic Anhydrase IX Expression of HT-29 Tumor Xenograft Mice with (68)Ga-Labeled Benzenesulfonamides. Mol. Pharm. 2016, 13, 1137–1146.
54. Yang, X.; Minn, I.; Rowe, S.P.; Banerjee, S.R.; Gorin, M.A.; Brummet, M.; Lee, H.S.; Koo, S.M.; Sysa-Shah, P.; Mease, R.C.; et al. Imaging of carbonic anhydrase IX with an 111In-labeled dual-motif inhibitor. Oncotarget 2015, 6, 33733–33742.
55. Yang, X.; Zhu, H.; Yang, X.; Li, N.; Huang, H.; Liu, T.; Guo, X.; Xu, X.; Xia, L.; Deng, C.; et al. Targeting CAIX with XYIMSR-06 Small Molecular Radiotracer Enables Noninvasive PET Imaging of Malignant Glioma in U87 MG Tumor Cell Xenograft Mice. Mol. Pharm. 2019, 16, 1532–1540.
56. Huang, W.; Wang, K.; An, Y.; Meng, H.; Gao, Y.; Xiong, Z.; Yan, H.; Wang, Q.; Cai, X.; Yang, X.; et al. In vivo three-dimensional evaluation of tumour hypoxia in nasopharyngeal carcinomas using FMT-CT and MSOT. Eur. J. Nucl. Med. Mol. Imaging 2020, 47, 1027–1038.